Ground Sky Imager Based Short Term Cloud Coverage Prediction

Stefan Hensel[1(✉)], Marin B. Marinov[2], Raphael Schwarz[1], and Ivan Topalov[2]

[1] Department for Electrical Engineering, University of Applied Sciences Offenburg, Badstraße 24, 77652 Offenburg, Germany
stefan.hensel@hs-offenburg.de
[2] Department of Electronics, Technical University of Sofia, 8, Kliment Ohridski Blvd., 1756 Sofia, Bulgaria
mbm@tu-sofia.bg

Abstract. The paper describes a systematic approach for a precise short-time cloud coverage prediction based on an optical system. We present a distinct pre-processing stage that uses a model based clear sky simulation to enhance the cloud segmentation in the images. The images are based on a sky imager system with fish-eye lens optic to cover a maximum area. After a calibration step, the image is rectified to enable linear prediction of cloud movement. In a subsequent step, the clear sky model is estimated on actual high dynamic range images and combined with a threshold based approach to segment clouds from sky. In the final stage, a multi hypothesis linear tracking framework estimates cloud movement, velocity and possible coverage of a given photovoltaic power station. We employ a Kalman filter framework that efficiently operates on the rectified images. The evaluation on real world data suggests high coverage prediction accuracy above 75%.

Keywords: Cloud coverage · High dynamic range images · Prediction algorithms · Short term irradiance prediction

1 Introduction and Motivation

Load forecasts have been an essential part of the management of electrical energy infrastructure and markets for decades. The integration of solar energy in the classical energy supply structures reduces the cost of generating power from other resources but at the same time introduces its own challenges and costs. Those challenges are mainly caused by the unstable conditions of regenerative energy sources. Main factor for the varying solar energy is the dynamic change of the sky conditions. Clouds are considered as one of the key elements in the sky which cause fluctuation in solar energy. A precise and short-term cloud coverage prediction is needed for a variety of applications primarily for the photovoltaic electrical power generation or for the alternative solar power plants whose electricity yield depends heavily on the cloud coverage of the sky. Light cloud cover of the sun already reduces generated power by up to 30% as

V. Poulkov (Ed.): FABULOUS 2019, LNICST 283, pp. 372–385, 2019.
https://doi.org/10.1007/978-3-030-23976-3_33

compared to cloudless conditions. If the light of the sun is dimmed by dense clouds, the yield could decrease by more than 75% [1].

The numerical weather prediction and the state-of-art geostationary satellite-based forecast approaches are restricted by their spatial and temporal resolution and are too rough for very short-term forecast applications. In this context, forecast approaches based on ground based sky imager are very promising as they provide high temporal and spatial resolution hemispherical information of the cloud cover [2, 3].

The choice of solar radiation forecast method depends strongly on the time periods which may vary from the perspectives of a few days in advance (intraweek), a few hours (intraday) or a few minutes (intrahour). Depending on the forecasting application different time horizons are relevant.

For very short time period of about 5–30 min, a number of techniques based on sky images have been developed for both Global Horizontal Irradiance (GHI) and Direct Normal Irradiance (DNI) prediction using cloud positioning information and deterministic models [2, 4].

For time horizons of 1–2 h, forecasting applications tend to be more statistical approaches such as autoregressive integrated moving averages [3].

One of the main advantages of sky imaging using large, ground based sensor network is that with only one or with a couple of cameras positioned in the zone of interest the actual cloud coverage can be determined with high resolution. The imaging systems can track cloud movements and can be used to reconstruct the spatial specificity of the clouds. With the current distribution and motion field, for about 5–30 min, future cloud configurations with high temporal and spatial resolution inside the forecast window can be predicted.

In contrast, a sensor network must be configured with a sufficiently close spacing throughout the zone of interest so that there is enough lead-time in the direction of cloud movement.

In most cases this scenario cannot be achieved due to cost reasons. Long-term, high-quality solar radiation data from ground sensors are vital for applications such as resource estimation and performance modelling. However for short-term forecasts, sky-imaging systems are more promising [3].

Short-term prediction of cloud coverage can generally be divided in two steps. The first involves the detection and the segmentation of clouds using available images. This one is of great importance since the quality of the second step, the actual prediction, depends on the most detailed representation of the clouds possible.

2 Approach and Tools

2.1 Camera

In this study, a ground-based sky camera is used to monitor the sky. It is mounted on the roof of the University of Applied Sciences Offenburg (Fig. 1).

Fig. 1. The camera system mounted on the roof of the University of Offenburg [5]

The sky camera is based on basic SkyImager-Designs as for example in [6] or [7, 8], and is pointed directly at the sky. A CCD sensor from Kodak and a 180° circular fisheye lens from Sigma Lens are used. As part of a testbed system, temperature and solar irradiance are measured [5]. This camera uses a fisheye lens with an angle of view of 185°. This results in a distortion of the imaged objects as shown in Fig. 2.

The lens curves the lines of the chessboard which in reality are straight. Similarly the actual straight path of a cloud is curved by the lens which makes subsequent tracking and cloudiness prediction much more difficult. Furthermore the movement of a cloud in the edge area of the shot in reality corresponds to a significantly greater distance compared to the same movement in the center of the picture. It is therefore useful to perform a distortion correction of the used images in a further pre-processing step and thus facilitates the subsequent prediction.

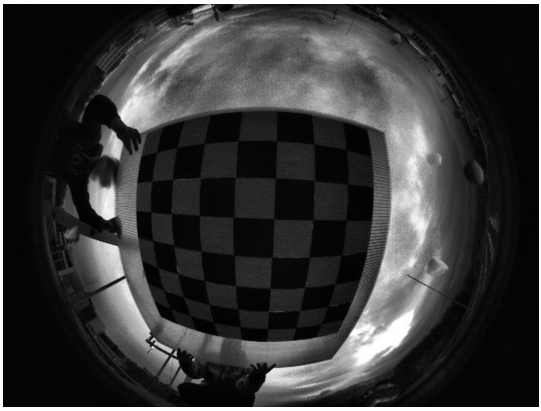

Fig. 2. Distortion of a chessboard by the fisheye lens

2.2 Calibration Principles

The principle of calibration is based on the Unifying Theory for Central Panoramic Systems of Geyer and Daniilidis [9] which states that any catadioptric and perspective projection can also be produced by imaging a three-dimensional sphere centered in the effective pixel.

The search for the transfer function of the lens connecting the three-dimensional coordinates of a point in the object space with the coordinates of its image in the plane of the image sensor is crucial for the image conversion algorithm. The task of finding the transfer function is solved by calibrating the omnidirectional optical system.

There are many methods for calibrating omnidirectional optical systems. One of the more detailed comparisons of these methods is given in [9, 10]. Out of the many methods of calibration, considered by the authors, a group of four methods available in the form of open source tools was highlighted.

1. Use of a spherical model of the camera; several images of a two dimensional test object are needed for calibration [11].
2. Use of a spherical model of the camera; A three-dimensional test object, consisting of three perpendicular test objects in the form of a chessboard is used for calibration [12].
3. A spherical camera model is also used. One camera image containing at least 3 lines is taken for calibration [13].
4. Omnidirectional images are considered distorted, the parameters must be calculated. Objects in the form of a chessboard are used for calibration [14].

The third technique, however, does not work with super-wide fisheye lenses. The rest three methods have approximately the same indicators of the calibration accuracy which are sufficient for solving the problem.

A technique is needed that would not require special technical equipment and could also be performed by unskilled personnel (or user of the system). In view of this the Scaramuzza method was chosen as the simplest and most convenient one for practical use.

The technique is implemented in the form of "OCamCalib" toolkit for MATLAB environment. To perform the calibration it is necessary to take several images of the test object in the form of a chessboard using a calibrated optical system. A further calibration process is practically completely automated. The calibration results are the calculated parameters (such as center coordinates and polynomial coefficients) for two functions defining a direct connection between the three-dimensional coordinates of the point in the object space and the coordinates of its image in the coordinate system of the image sensor $((u', v')) = world2cam(x, y, z)\ and\ ((x, y, z)) = cam2world(u', v')$. The calibration process is described in detail in [13–15].

The underlying model does only the reposition of the pixels on the image plane with an assumed distortion function. Additionally a vector $(\mathrm{x}, \mathrm{y}, \mathrm{z})^{\mathrm{T}}$ is computed radiating from the single viewpoint to a picture sphere pointing in the direction of the incoming light ray for each pixel position $(\mathrm{u}, \mathrm{v})^{\mathrm{T}}$. This reference frame originates in the center of the image.

The radial distortion is defined as a Taylor polynomial with Function F(ρ) given as

$$F(\rho) = \mathrm{a}_0 + \mathrm{a}_1\rho + \mathrm{a}_2\rho^2 + \mathrm{a}_3\rho^3 + \ldots + \mathrm{a}_\mathrm{n}\rho^n \tag{1}$$

$$\rho = \sqrt{u^2 + v^2}. \tag{2}$$

The coefficients a_i define the intrinsic parameters and the Euclidean distance of the pixel position $(u, v)^T$ from the image center and is defined by Eq. (2). The latter is needed to make use of the spherical projections properties so that a point in camera coordinates can always be represented as a point on a specific ray. This is expressed in Eq. (2) with c being an arbitrary scaling factor.

$$\begin{pmatrix} x \\ y \\ z \end{pmatrix} = c \begin{pmatrix} u \\ v \\ F(\rho) \end{pmatrix} \tag{3}$$

To project a point from camera coordinates onto an image the parameters of Eq. (3) has to be determined in order to get u and v. The calculation is based on a least squares criterion and is done for the overdetermined system with singular value decomposition.

2.3 Distortion Correction by Interpolation

Once the parameters have been determined for the camera in use the distorted images can now be transformed to an area-consistent perspective. This is achieved with a simple interpolation [16]. With this function the input image V at the coordinates of the distorted fisheye sampling points in X and Y is interpolated to the coordinates of the undistorted equirectangular points in Xq and Yq. The result Vq is the undistorted image. X and Y correspond to the pixel coordinates of the image used. The two matrices Xq and Yq are determined with the help of a function that needs as input a three-dimensional point as well as the calibration parameters of the camera.

Each 3D point is composed of X and Y image coordinates of the point to be undistorted and the negative Z coordinate N_Z where N_Z corresponds to the assumed focal length of the camera.

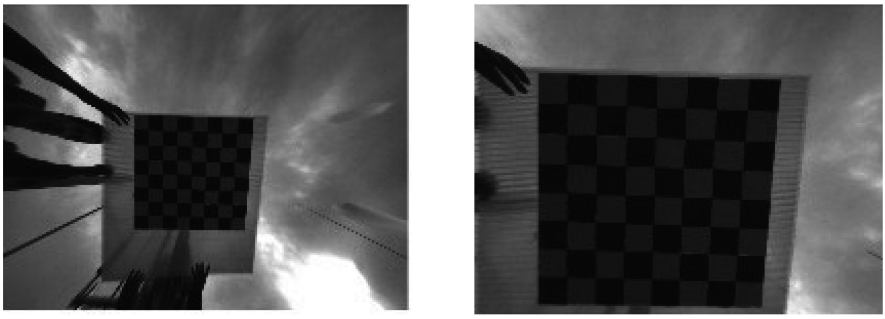

a) b)

Fig. 3. Distortion correction of the image from Fig. 2, with (a) $N_Z = -300$ and (b) $N_Z = -600$

Figure 3 shows the result of the interpolation for two different values of N_Z. The distorted lines of the chessboard in the input image are straight lines on the output images as desired. Higher values of N_Z increase the close-up details but restrict the field of view as shown in Fig. 3(b). Values that are chosen smaller increase the distortions of the equirectangular transformation in the areas towards the image borders which can be seen in Fig. 3(a). The proposed procedure is fast and completely automatic as the user is only asked to collect a few images of a checker board and to click on its initial corner point. The only assumption is that the lens can be modeled by a Taylor series expansion of a unified spherical perspective model (For further details we refer to [17]). It should be noted that distortion correction is performed for each of the three RGB channels independently and then the channels are recombined into the undistorted RGB image.

The aim of the pre-processing step is to prepare the images of the fisheye camera for subsequent detection of the position of the sun, then to perform segmentation of the clouds and finally to determine the movement of the clouds in order to predict a possible reduction in solar power generation. If the lens parameters are known the transformation from fisheye images to an equirectangular representation shifts the problem of trajectory estimation from a non-linear motion model of changing radial patterns of the clouds to a *linear system* that can be tackled with efficient algorithms, e.g. the Kalman Filter.

3 Sun Path Calculation and Cloud Segmentation

3.1 Sun Position Calculation

The zenith and the azimuth angles of the sun at a particular time can be calculated using the longitude, latitude and altitude of the desired location as well as any date and time [18, 19]. A zenith angle of 0° corresponds to the maximum possible zenith, 90° sunrise or sunset. If these two angles are known the sun's XY position on the distorted HDR image, when these two angles are known, can be calculated using the following formulas:

$$x_{sun} = r_{sun} \cdot cos(\varphi_{sun}) + \frac{width_{pic}}{2} \tag{4}$$

$$y_{sun} = r_{sun} \cdot sin(\varphi_{sun}) + \frac{height_{pic}}{2} \tag{5}$$

The azimuth angle of the sun is presented with the angle φ. The orientation of the camera should be taken into consideration and thus the computed value based on the Sun Position function should be shifted producing next correction for the images used here:

$$\varphi_{sun} = -Azimuth_{sun} + 164.2484 \tag{6}$$

The required radius r_{sun} can be determined by the calculated zenith angle for this purpose - the corresponding distance in pixels of the sun to the center of the image is

measured several times at every possible zenith angle. For a given zenith angle the corresponding radius can be read out via this table.

Figure 4 shows the calculated sun path for the months of January, March, May, July, August and October. As expected, the position of the sun is much lower in the winter months than, for example, as shown in the figures. Going to the image edges leads to a bigger sun distortion in the rectified HDR images. For the upcoming steps it would be more difficult to separate the sun from the cloud shapes which would rely on rectified images.

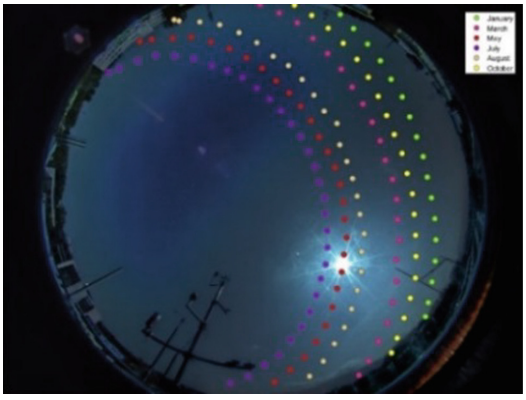

Fig. 4. Sun path during the year over the Offenburg University

3.2 Segmentation of Clouds and Sky

To segment clouds from clear sky we use the so-called Red-Blue Ratio (RBR) which only relies on the red and blue color channel [13]. In addition to the RBR with fixed parameters a dynamic and local thresholding scheme analogue to [14] is used.

1. **RBR value and Clear-Sky Image (CSI).** The physical scattering of wavelengths is the source for the RBR and this is the reason that the skies are colored in blue and clouds in different shades of gray. The ratio is calculated with

$$RBR = \frac{R}{B} = 1 + \frac{R - B}{B}. \tag{7}$$

The segmentation of thick clouds from clear sky is easy. But the common case of thin layered or wispy clouds, so called cirrus clouds, or the combination of thick and thin clouds against the sky is a hard task only relying on a single threshold. The problem is depicted in Fig. 5 coverages from thick to thin, emphasizing the problem of choosing a sensible threshold for segmentation. Besides cloud thickness, the inhomogeneity of the sky poses the biggest problem for thresholding methods. The RBR value of a clear sky, when reaching the sun and horizon, increases. In order to escape

incorrect detection of sky pixels as clouds the clear sky RBR_{CSI} value is subtracted from the current value of RBR of the HDR image RBR_{HDR}.

$$RBR_{diff} = RBR_{HDR} - RBR_{CSI}. \tag{8}$$

This renders the resulting RBR spectrum independent of the actual influence of sky illumination. A prerequisite for the subtraction is the availability of clear sky images for every time of the year. Since this is hard to come by (except in some desert regions), we choose to generate the ideal clear sky image based on a physical model.

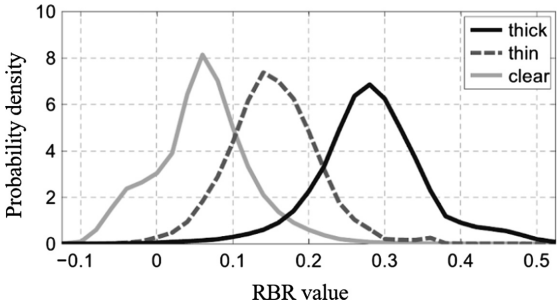

Fig. 5. Typical RBR values (image adapted from [3])

2. **Calculation of CSI values.** In order to have a calculated CSI image we used the methods described in [3]. Based on the CIE Standard Clear Sky model [20], the color intensity L of the clear sky is calculated as a function of the sun pixel angle (SPA) and the pixel zenith angle (PZA) using the following formula:

$$I_p(PZA, SPA) = \underbrace{\alpha_1 \cdot \left[1 + exp\left(\frac{a_3}{cos(PZA)}\right)\right]}_{=f_1(PZA)} \cdot \underbrace{\left[a_4 + a_5 \cdot SPA^{a_6} + a_7 \cdot cos(SPA)^2\right]}_{=f_2 SPA} \tag{9}$$

The luminance and subsequently the color values of the presumed clear sky could be computed if the parameters a_1 to a_7 are known. With the help of this the *PZA* and *SPA* values are converted from the x-y-coordinates. The *PZA*, denoted by *Z* in Fig. 6, is determined as the distance of the pixel to the center of the fisheye image.

The CSI for each pixel can be computed only when all seven parameters for the three color channels have been calculated using Eq. (10):

$$CSI = \left(a_1 PZA^2 + a_2 PZA + a_3\right) \cdot \left(a_4 SPA^3 + a_5 SPA^2 + a_6 SPA + a_7\right) \tag{10}$$

A model of a Clear Sky Image has been created by computing a function for the intensity of each pixel based on its position. This CSI image is used for the separation of the clouds from the sky.

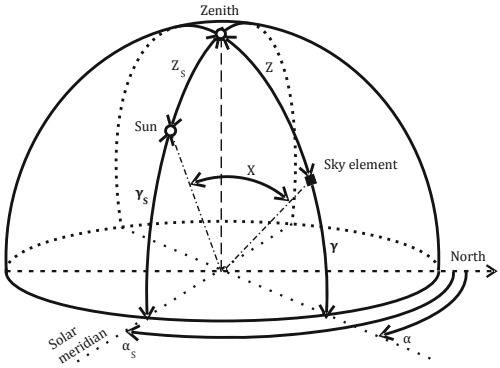

Fig. 6. Angle definitions for object positioning in the sky [20]

For cloud discovery two diverse approaches have been used. The first one is *fixed red blue ratio threshold* and the second one is a *dynamic gray scale threshold*. All images are sharing the same determined RBR threshold. A universal threshold for the given image is calculated with the help of the algorithm for gray scales values of the difference between HDR image and CSI. Extremely adequate results are obtained from both algorithms for diverse scenarios: the method based on RBR obtains good results in separating ticker and darker clouds while the gray scale method obtains weaker results. For improving the output of thinner clouds, the results are inverted and the gray scale threshold performs better than the RBR method. For the occasion when there are different parts of clouds both methods are used which produce reasonable results.

The described process of cloud separation should be considered as a middle step of short time solar power forecast. A throughout calibration and tuning should be done of the camera and the HDR images. After this process, an algorithm for prediction of the movement of the clouds should be used, in our case a model-based estimation in a multi assumption domain. The gray value algorithm was chosen for our research although both processes produce proper results because its separation results are good and the output of the separation deliver the information for the clustering and separate cloud movement forecast using monocular camera images. Further details and exemplary results are shown in [21].

4 Tracking

In this chapter the final short-term prediction of the before segmented cloud coverage is explained.

For the detection and tracking of multiple objects on a motionless background in the video stream of a stationary camera for personal or traffic monitoring, a multiple object tracking (MOT) method is often used. In this method an individual trajectory (track) is created for each newly detected object on an image or frame. On the next frame, the objects are detected again but are now assigned to the existing tracks of the

previous frame. The time between two frames for our camera system is limited to last 30 s, to allow for the taking of four exposure rows.

If one or more detected objects cannot be assigned to existing tracks, a new track will be created for them. The assignment is done exclusively through the position and movement of the objects and their center of gravity using the Kalman filter as model based estimator. The Kalman filter estimates the velocity and position of the object based on previous states. The underlying physical model allows the prediction of the actual and following time step and the actual cloud position which is then used to assign the detections in a more robust manner.

We assume the constant velocity model for the prediction and correction steps which proved the best correspondence with the actual observed cloud movement.

4.1 Kalman Filter

To reliably track an object through a series of images, its position for the current image must be estimated from previous positions and observations. A well-established approach for estimation and prediction of moving objects is the Kalman filter which estimates the current position of an object based on former states and associated observations that are combined based on a physical motion model. For this contribution several motion models were evaluated and the constant motion model was chosen heuristically matching actual cloud movement. The equirectangular projection of the fisheye image results in a linear cloud movement along the sky which allows the employment of the basic Kalman filter without the need of designing a non-linear motion model and henceforth using the non-linear filter derivatives as an unscented Kalman filter or particle filter.

The Kalman Filter is a twostep algorithm based on the predictor corrector scheme. In the first step, the current position of the object is estimated from the previous positions and the corresponding error covariance. Then, in the second step, the estimated position and the error covariance are corrected by measurement. The advantage here is that even if the position cannot be corrected one or more times by observations, the corrections are still performed using the information from previous states and motion model. The predictions are thus becoming more inaccurate the further in time the actual state is predicted. New measurements then correct the state and covariance again. The results of the filter estimation are shown exemplary in Fig. 7 for two consecutive frames. All detected cloud objects are numbered and indicated by a yellow box. The estimated position is shown by the red centroid and the blue vector visualizes the velocity, albeit scaled by a factor of ten.

Since each segmented and detected cloud is treated as an independent object, one instance of a Kalman filter is created for each cloud leading to a multi hypothesis approach for object tracking. As cloud position we define the centroid (center of gravity) of the object which yields a higher distance to neighboring clouds and lies within a relatively homogeneous area of the cloud; velocity is determined in multitudes of pixels as the shift of the centroid between the frames. The correction step of the tracker framework uses the velocity as observation giving rise to the question of appropriate data association for the cloud objects between the frames.

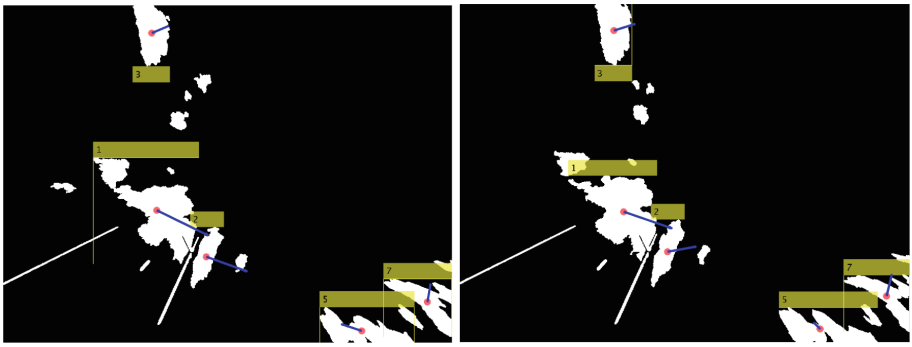

Fig. 7. Estimation of cloud position and velocity by multiple Kalman filters. Position of object is determined by the red dot, the estimated velocity by the blue vector, scaled with a factor of ten. (Color figure online)

4.2 Tracking Routine Implementation

For the tracking routine, management of the detected tracks is of utmost importance. To prevent misdetections, the tracks must be detected on a minimum number of frames before they are defined as a reliable object. At the same time, tracks that exist too long without updated measurements in the form of an associated detection must be deleted. As a result, the clouds that dissolved or left the image area are no longer pursued.

The software framework consists of two main parts. The first part initializes and manages tracks based on detected centroids.

Therefore each Kalman filter uses a detected centroid as starting position to initialize the track. Each filter has an associated lifetime indicating the frames in which its object was visible and an associated counter that determines whether a track has not been detected for too long and thus can be deleted.

The second part of the program is cyclically repeated for each new high dynamic range image from the exposure series. A binary cloud mask is created for the rectified HDR image as described in Sect. 3 and the current position of the Sun is calculated.

In the following data association step, all current detections are assigned to already existing tracks. The subsequent assignment is implemented as a Hungarian assignment method based on the variant described in [22].

Exemplary results for the Track management of diverging or appearing cloud objects are shown in Fig. 8. The larger cloud numbered 11 on the left side of the image is dividing and assigned two new objects on the right side namely 10 and 11.

4.3 Experimental Results

The presented algorithm was tested on several hundred images taken from different sequences containing individual weather conditions. Segmentation and initialization of the multi hypothesis tracker works reliable in all considered conditions. A demonstrative example is shown in Fig. 9. The framework is presented with two frames and associates the detected cloud centers. In the third frame all tracks are initialized with an individual Kalman filter indicated by the yellow bounding boxes and the corresponding centroid.

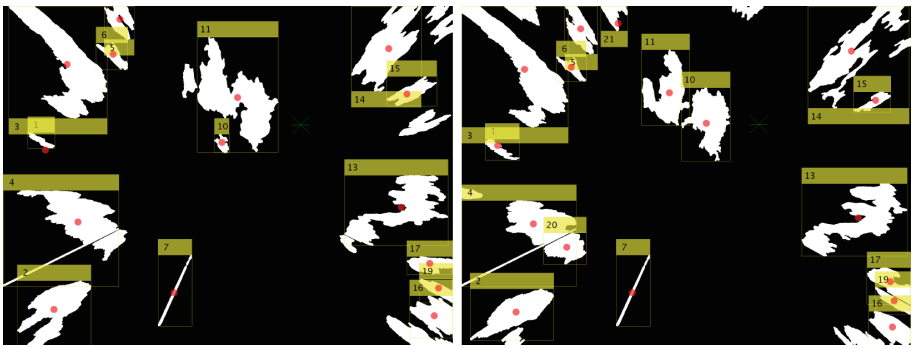

Fig. 8. Track management for diverting clouds. The cloud object 10 on the left side dissolves whereas the cloud object 11 on the left side splits up into two new objects, 10 and 11, on the right side.

Fig. 9. Initialization of Kalman filters for a given detection sequence. All cloud objects are kept by data association in the first two frames indicated on the left and in the middle. Each tracked object is shown on the right image given by its bounding box and centroid.

Short Time Cloud Coverage Prediction

An example for the prediction of the cloud object is shown in Fig. 10. The blue object in the right image indicates the predicted position after 12 frames which corresponds to six minutes. The considered object is numbered with the bounding box five.

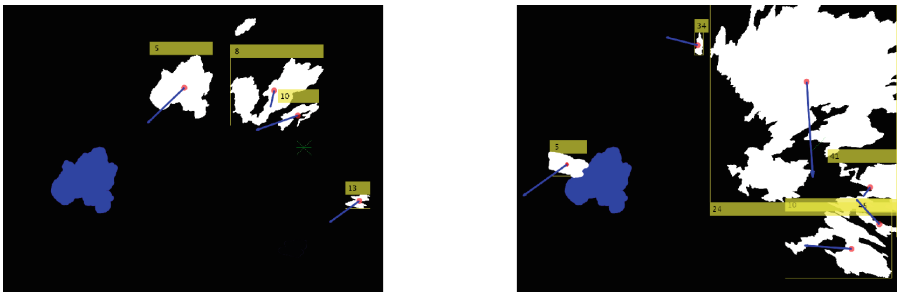

Fig. 10. Short time prediction of cloud objects. The blue shape indicates the predicted position of cloud number five of the left image. After six minutes the shape has changed but the prediction was quite accurate. (Color figure online)

Although the shape of the cloud is changing noticeably it is robustly tracked and the prediction is relatively accurate for the purpose of sun coverage prediction.

The accuracy of coverage was tested with two cloudy sequences from 2nd March 2017, comprising 216 images. For the given sequences there have been 47 cases where the sun became covered by a moving cloud. We predicted the time of five minutes and evaluated prediction with real coverage. From the 48 coverage events 37 have been correctly predicted and 11 were not. This gives an accuracy of prediction of 77%.

5 Conclusion

Understanding the needs for short-term forecasts are growing as utilities and grid operators gain experience in managing solar-power sources. The use of sky images for providing forecasts over a local spatial area has the potential to provide, at a competitive price, an accurate, high-resolution, short-term forecast needed for efficient power generation, transmission and distribution.

In this paper we present a novel approach of short time cloud coverage prediction for the purpose of solar power optimization. Our approach is based on two stages where at first the clouds are segmented from clear sky by using rectified HDR images in combination with a color based thresholding and model based clear sky simulation. In the second stage, we use a multi hypothesis Kalman filter framework to track each segmented cloud estimating current position and velocity. With this information, a short time prediction within roughly ten minutes can be given to assess the possibility of clouds moving over the sun and thus shorten the photovoltaic power output.

Acknowledgments. This paper has been produced within the framework of the ERASMUS + project Geothermal & Solar Skills Vocational Education and Training (GSS-VET).

References

1. Sun, S., et al.: Short term cloud coverage prediction using ground based all sky imager. In: IEEE International Conference on Smart Grid Communications (2014)
2. Chow, C.W., et al.: Intra-hour forecasting with a total sky imager at the UC San Diego solar energy testbed. Solar Energy **85**(11), 2881–2893 (2011)
3. Kleissl, J.: Solar Energy Forecasting and Resource Assessment. Academic Press, Oxford (2013)
4. Marquez, R.; Coimbra, C.: Short term DNI forecasting with sky imaging techniques. In: Proceedings of the American Solar Energy Society, Rayleigh, NC (2012)
5. Kömm, T.: Entwicklung einer Wolkenkamera zur Kurzzeitvorhersage von Solarenergie. University of Offenburg, Offenburg (2016)
6. Kleissl, J., Urquhart, B.: Sky imager cloud position study field campaign report. University of California, San Diego (2016)
7. Cazorla, A., Olmo, F.J., Alados-Arboledas, L.: Development of a sky imager for cloud cover assessment. J. Opt. Soc. Am. A **25**(1), 29–39 (2008)

8. Gauchet, C., Blanc, P., Espinar, B., Charbonnier, B., Demengel, D.: Surface solar irradiance estimation with low-cost fish-eye camera. In: Workshop on Remote Sensing Measurements for Renewable Energy, Risoe, Denmark (2012)
9. Geyer, C., Daniilidis, K.: A unifying theory for central panoramic systems and practical implications. In: Vernon, D. (ed.) ECCV 2000. LNCS, vol. 1843, pp. 445–461. Springer, Heidelberg (2000). https://doi.org/10.1007/3-540-45053-X_29
10. Paniagua, C., Puig, L., Guerrero, J.J.: Omnidirectional structured light in a flexible configuration. Sensors **13**(10), 13903–13916 (2013)
11. Mei, C., Rives, P.: Single view point omnidirectional camera calibration from planar grids. In: Proceedings of IEEE International Conference on Robotics and Automation, ICRA 2007, Rome, Italy (2007)
12. Puig, L., Bastanlar, Y., Sturm, P., Guerrero, J.J., Barreto, J.: Calibration of central catadioptric cameras using a DLT-like approach. Int. J. Comput. Vis. **93**(1), 101–114 (2011)
13. Barreto, J.P., Araujo, H.: Geometric properties of central catadioptric line images and their application in calibration. IEEE Trans. Pattern Anal. Mach. Intell. **27**(8), 1327–1333 (2005)
14. Scaramuzza, D., Martinelli, A., Siegwart R.: A flexible technique for accurate omnidirectional camera calibration and structure from motion. In: Proceedings 4th IEEE International Conference on Computer Vision Systems, ICVS 2006, NY, USA (2006)
15. Scaramuzza, D., Martinelli, A., Siegwart, R.: A toolbox for easily calibrating omnidirectional cameras. In: Proceedings of IEEE International Confernce on Intelligent Robots and Systems, IROS 2006, Beijing, China (2006)
16. Corke, P.: Robotics: Vision and Control: Fundamental Algorithms in MATLAB, 2nd edn. Springer, Cham (2017). https://doi.org/10.1007/978-3-319-54413-7
17. Hensel, S., Marinov, Marin B., Schwarz, R.: Fisheye camera calibration and distortion correction for ground based sky imagery. In: Proceedings of XXVII International Scientific Conference Electronics – ET 2018, Sozopol, Bulgaria, 13–15 September 2018 (2018)
18. Reda, I., Andreas, A.: Solar position algorithm for solar radiation application, Technical report, National Renewable Energy Laboratory (2008)
19. Asparuhova, K., Djamiykov, T., Spasov, I.: Research and design of effective positioning algorithm for solar tracking system. In: IX National Conference with International Participation (ELECTRONICA), Sofia (2018)
20. Kittler, R., Darula, S.: Cie general sky standard defining luminance distributions. In: Proceedings of Conference eSim 2002. The Canadian Conference on Building Energy Simulation (2002)
21. Hensel, S., Marinov, Marin B., Schwarz, R., Ganev, B.: Algorithms for cloud segmentation with ground-based camera images. In: Proceedings of International Conference Balkan Light 2018, Varna, Bulgaria, 20–22 September 2018 (2018)
22. Munkres, J.: Algorithms for the assignment and transportation problems. J. Soc. Ind. Appl. Math. **1**(5), 32–38 (1957)